Supplementary Information

Kinetically-controlled laser-synthesis of colloidal high-entropy alloy nanoparticles

Friedrich Waag,[a] Yao Li,[a] Anna Ziefuß,[a] Erwan Bertin,[a] Galina Marzun,[a] Marius Kamp,[b] Viola Duppel,[c] Lorenz Kienle,[b] Stephan Barcikowski[a] and Bilal Gökce*[a]

[a] Technical Chemistry I and Center of Nanointegration Duisburg-Essen (CENIDE), University of Duisburg-Essen, 45141 Essen, Germany. E-mail: bilal.goekce@uni-due.de

[b] Synthesis and Real Structure, Kiel University, Institute for Materials Science, 24143 Kiel, Germany.

[c] Nanochemistry, Max Planck Institute for Solid State Research, 70569 Stuttgart, Germany.

DOI: 10.1039/c9ra03254a

1. Laser synthesis of CoCrFeMnNi high-entropy alloy nanoparticle colloids

At first, the simplified process chain of the synthesis of heterogeneous catalysts based on laser-synthesized CoCrFeMnNi HEA nanoparticle (NP) colloids is presented in Figure S1. The process started at the single metal micropowders. It included the steps of weighting, grinding and mixing, pressing, heat-treating and laser ablating. Laser ablation yielded NPs, which were immobilized on carbon black (CB) to produce heterogeneous catalysts. Figure S2 presents size distributions of laser-generated HEA NPs by TEM analysis. Slight differences showed up between the sample synthesized in ethanol and that synthesized in the upscaling approach, with a tendency to smaller particles for the ethanol-based synthesis. However, the average Feret diameter was smaller than 2 nm in both cases.

2. Crystal structure analysis

The crystal structure of the mixture of the single metal micropowders and different ablation targets was investigated. Beside 20 h of target heat-treatment duration at 1,000 °C, three different durations, namely 0.33, 5 and 50 h, were applied to investigate the effect on the CoCrFeMnNi HEA lattice formation due to diffusion. For each heat-treatment duration, three metal sheets were heat-treated. After heat-treating, all targets were sanded to remove oxide layers on their surfaces.

The micropowder pellets heat-treated at 1,000 °C for different heat-treatment durations as well as the mixture of Co, Cr, Fe, Mn and Ni micropowders were characterized by XRD. For XRD analysis, all targets were rasped to powders. The obtained raw data was analyzed using the program “MAUD” (M. Ferrari and L. Lutterotti).

Figure S3a shows the XRD patterns of the ablation targets. Mainly three peaks showed up indexed as the (111), (200) and (220) planes of an fcc lattice, which was expected to form for the CoCrFeMnNi HEA. Besides those three peaks, only minor diffraction peaks were found, which could be assigned to a spinel-like oxide. Further information on the oxide phase can be found in the main manuscript. The results from XRD proved the ablation targets had no significant crystalline impurities. Interestingly, the ablation targets heat-treated for only 20 min (holding time) at 1,000 °C already possessed the desired crystal structure. In contrast, the

XRD pattern of the mixture of the metal powders exhibited diffraction peaks of different phases. A zoom into the region of 40 to 60° 2 Theta is shown in Figure S3d.
The reflections of the (111) planes of the ablation targets were fitted using Gaussian peaks (Figure S3b). The ratio of FWHM and peak height changed with a longer heat-treatment duration, which implied a change in the crystallite size of the CoCrFeMnNi HEA in dependence on the heat-treatment duration. This was confirmed by calculating their crystallite sizes using the Scherrer-equation (Figure S3c).[S1] The crystallite size changed up to a heat-treatment duration of 20 h.
In summary, the ablation targets were successfully synthesized with a single solid solution phase of the CoCrFeMnNi HEA and a negligible oxide phase. However, to achieve the solid solution phase of the CoCrFeMnNi HEA, a heat-treatment duration of only 20 min at 1,000 °C was sufficient. However, a heat-treatment duration of 20 h was used for further experiments of this work. The crystallite size significantly changed up to 20 h sintering and remained nearly unchanged afterwards.
The Σ3-twin formation in some larger NPs indicated by XRD (Figure 3) and SAED (Figure 4b,h,i) was further investigated by HRTEM. A representative atomic lattice and the corresponding FFT are shown in Figure S4.

3. Chemical composition

The investigation of the chemical composition of single NPs revealed a surface segregation of Cr and Mn in some larger NPs, which also showed a formation of Σ3-twins. EDX elemental mapping of the surface region of a single NP is shown in Figure S5. The results demonstrated the selective segregation of Cr and Mn.
A part of a laser ablation area on the surface of a CoCrFeMnNi HEA target was investigated by EDX (Figure S6). Apart from single areas in which Cr was obviously concentrated, all elements were homogeneously distributed in the rest of the investigated area.
In order to examine the purity of the used powders, EDX elemental analysis of each single powder was performed. Figure S7 shows the EDX spectra of all five powders. Beside signals of the corresponding element, each spectrum consisted peaks related to C, Al and Cu, all contributed by the sample holder and the used carbon fixation pads. Furthermore, small peaks corresponding to oxygen appeared in the spectra. This indicated slight oxidation of all powders. However, a contribution by the fixation pads could not be excluded.
Figure S8 presents SEM images of the five metal powders used for preparing ablation targets of the CoCrFeMnNi HEA. Particles of the Co powder were aggregated and formed long rods and other irregular shapes. The corresponding particle size histogram of the Co powder considered the width of the rods. A narrow size distribution with a mean particle size of about 0.7 µm was found (Figure S9a). In comparison, the Cr powder consisted of chip-like particles (Figure S8) with a larger mean diameter of 1.6 µm and a broader particle size distribution (Figure S9b). The Fe powder consisted of spherical particles (Figure S8) and exhibited a similar size distribution as the Cr powder (Figure S9c). The Mn powder (Figure S8) exhibited non-uniform particle morphologies with some irregular shaped particles of significantly larger size compared to others. This was also depicted by the corresponding particle size histogram

(Figure S9d). In addition, most of particles of the Ni powder were of a near-spherical shape with rough surfaces (Figure S8). A relatively broad size distribution with a mean diameter of about 2.5 µm showed up (Figure S9e). It can be seen from Figure S8 that some single particles were merged to aggregates. In this work, the single powders were mixed and grinded for 20 min. SEM investigation of the grinded mixture (Figure S8) demonstrated well mixed particles. EDX analysis underlined the good mixing state of the five metal powders. However, several fractions with relatively higher concentrations of Mn and Ni appeared, which was attributed to the observed larger primary particles of Mn and the aggregates of Ni.

Figure S11 presents an exemplary SEM image of an ablation target before the laser ablation. The striped surface structure was formed by sanding to remove the oxide layer, which was generated during the heat-treatment. The homogeneity of the chemical composition of the target as determined by EDX mapping is also presented in Figure S11. It can be seen that each of the five elements was evenly distributed throughout the target. For each produced target, three different positions of the target surface were mapped for the five single metals by EDX. (The results are not shown here, because they are similar to those presented in Figure S11.) This implied that the target heat-treatment duration of 5 h already sufficed to obtain a uniform distribution of the five elements.

Figure S12 presents the EDX spectrum of an ablation target heat-treated for 20 h. Clear signals for all metals, namely Co, Cr, Fe, Mn and Ni can be observed. Furthermore, peaks for C, O and Si were detected in the spectrum. The targets were stored on a silica slide during heat-treating. Consequently, Si could diffuse into the ablation target.

4. Scale-up of the laser-synthesis of high-entropy alloy nanoparticles

The scale-up of the laser-based HEA NP synthesis was performed as described in the main manuscript. Here, we only want to present TEM images of the HEA NPs synthesized in the scale-up approach. The morphologies of the NPs synthesized in the scale-up (Figure S13c,d) differ not from those synthesized in ethanol (Figure S14a,b). However, the size distribution shifted towards larger diameters (Figure S2). It is obvious from Figure S14b that a higher degree of surface oxidation of the particles occurred in the water-based, upscaled synthesis.

5. Catalyst preparation

Colloidal NPs were mixed with CB, which was dispersed in the same liquid as was used for the laser synthesis. Subsequently, the colloidal support suspensions were shaken for 5 min and treated with ultrasonic for 15 min. Due to the high stability of the as prepared HEA catalysts (20 wt.%) in ethanol, the solvent was evaporated at room temperature to obtain the heterogeneous catalyst shown in Figure S14. In case of using water, the catalysts sedimented within 24 h. Catalysts with 10, 40, 60 and 80 wt.% HEA NPs were also prepared. Furthermore, HEA catalysts (20 wt.%) with other support materials, namely graphene oxide (GO), graphene nanosheets (GNS) and nitrogen-doped graphene nanosheets (N-GNS) were prepared by applying the same procedure. The electrochemical performance is shown in Figure S22.

For a comparison of the activity of catalysts based on HEA NPs, ablation targets of alloys of cobalt and nickel (Figure S15a) were prepared and ablated under the same conditions.

Catalysts prepared from the ablation products showed a synergistic redox behavior during cyclic voltammetry (Figure S15b).

6. Reproducibility of the laser-based synthesis

To investigate the reliability of the laser-based synthesis of NPs from targets of the CoCrFeMnNi HEA, a reproducibility study was carried out. Therefore, samples of NP colloids produced under various conditions of the laser-based process were investigated by UV-Vis extinction spectroscopy (Figure S16-20). From chosen samples, catalyst were prepared and electrochemically investigated. The results are shown in Figure S21-22 and discussed later.

6.1. Volume flow

In order to find a suitable volume flow rate for the laser ablation using a flow chamber, an ablation target of nickel was ablated at different volume flow rates (Figure S16a). To determine and compare the ablation efficiencies at different volume flow rates, the extinctions at 350 nm, 500 nm and 700 nm of a colloid produced at 5 ml/min were used as base value. The corrected extinctions E_c for colloids produced at higher volume flow rates were calculated by the Equation (S1), in which E_0 is the normal extinction of a sample at a particular wavelength and F the volume flow rate used for the preparation of the sample.

$$E_c = \frac{F}{5\ \mathrm{ml/min}} * E_0 \qquad \text{(S1)}$$

Figure S16b shows that the sample obtained at 20 ml/min exhibited the highest corrected extinction at each wavelength. This implied that the most efficient volume flow rate, which enabled the highest NPs production rate, was 20 ml/min. Further investigations were carried out by using this flow rate.

6.2. Investigation of the impact of ablation duration

To investigate the change in the concentration of prepared NP colloids at increased duration of ablation, samples obtained at different time points in the process were investigated by UV-Vis extinction spectroscopy. It can be seen from Figure S17b that the UV-Vis extinction was stable from the 2nd minute of the laser ablation. This result is close to the theoretical value for the residual time of a volume element in the setup, which is 1.36 min and can be determined by (S2) using the volume flow rate (F) of 20 ml/min and characteristic lengths of the setup. A flow chamber with a length (L_{ch}) of 9.4 cm was used for the synthesis of colloids by laser ablation in this work. A tube with a length (L_{ho}) of 30 cm and an inner diameter (D_{in}) of 1 cm was connected to the ablation chamber to transport the generated colloid to a collecting vessel. Since the target was fixed and ablated in the center of the chamber, the average time (t) that a colloid volume unit needed to flow to the collecting vessel can be calculated by the following equation:

$$t = \frac{\pi * \left(\frac{D_{in}}{2}\right)^2 * \left(\frac{L_{ch}}{2} + L_{ho}\right)}{F} \qquad (S2)$$

$$= \frac{3.14 * \left(\frac{1\ \text{cm}}{2}\right)^2 * \left(\frac{9.4\ \text{cm}}{2} + 30\ \text{cm}\right)}{20\ \text{ml/min}}$$

In order to minimize the probability for deviations of the characteristic properties of NP colloids, samples were taken not earlier than 2 min after the start of the laser ablation process.

6.3. Investigation of the impact of the target heat-treatment duration

In order to examine the effect of the target preparation on the reproducibility of the laser-based synthesis of NP colloids from ablation targets of the CoCrFeMnNi alloy heat-treated for 5 h, 20 h and 50 h were prepared and investigated by UV-Vis extinction spectroscopy. For each heat-treatment duration, three targets were produced. One target of each heat-treatment duration was used to produce three samples by laser ablation in ethanol. UV-Vis extinction spectra were recorded. An exemplary extract of the obtained results is presented in Figure S18. Similar spectra resulted for all samples. The average extinctions (320 nm) of samples from targets heat-treated for 5 h, 20 h and 50 h are almost identical with a value of around 1.23 (Figure S18b). Moreover, the Furlong slope[S2] of all each sample spectrum was determined (Figure S18d). All calculated slopes of the samples of the nine targets were nearly identical. This indicated similar particle size distributions of all samples, although their concentrations differed slightly. Additionally, the extinction spectra of the samples were normalized by the extinction at 320 nm. Figure S18e shows that the spectra overlay each other after the normalization. Therefore, it can be concluded that the heat-treatment duration had no significant effect on the laser-based synthesis of NP colloids from ablation targets of the CoCrFeMnNi HEA in the investigated range.

6.4. Investigation of the impact of the focal plane position

In order to investigate the influence of the position of the focal plane during the laser ablation on the optical properties of the synthesized colloids, five different positions were realized. Five colloids were produced at each focal plane position and analyzed by UV-Vis extinction spectroscopy. Again, the extinctions at the wavelength of 320 nm were extracted from the spectra and plotted versus the positions of the focal plane. A position of the focal plane of 0 mm indicates the position at which the highest productivity was observed.

It can be seen from Figure S19a that all samples prepared at the position of 0 mm exhibited the highest extinctions in each measurement except measurement 5, in which the highest extinction was reached, when the focal position deviated by 0.5 mm. The average extinctions calculated from the results of all measurements are shown in Figure S19b. The diagram presents more obviously that an optimal distance of the target surface to the focal plane existed, which enabled a maximized NP productivity. However, effects of the variation of this distance in a range of -1 to 1 mm did not significantly vary the colloidal properties. This can be presumed from Figure S19c, which shows the corresponding, normalized extinctions (to those

measured for samples produced at 0 mm) at a wavelength of 320 nm. It is obvious that results for -1 mm, -0.5 mm, 0.5 mm and 1 mm differ from those for 0 mm only within a limited range of 10% in positive and negative direction. Moreover, Figure S19d presents the average Furlong slopes of the samples produced at different positions of the focal plane. All slopes were close to each other with a value of about -2.25. This implied that all samples prepared in this experiment exhibited a similar particle size distribution. However, a slight trend to smaller NPs was observed at more negative focal plane positions, which was likely due to laser irradiation of the colloidal NPs.

6.5. Investigation of the impact of repeated start in long-term ablation

The process stability during repeated restarts of the laser-based synthesis were also investigated. Samples of NP colloids were taken for UV-Vis extinction measurements in the 2nd and 10th minute of the laser-based synthesis. Samples from eight runs or restarts were analyzed to investigate the reproducibility. After 10 min of laser ablation, the laser radiation was stopped for 5 min, to allow cooling of the ablation target, and restarted again. It can be seen from Figure S20a that all samples taken after 10 min of laser ablation had a slightly higher concentration than those taken after 2 min. The extinctions of all samples were normalized by the extinctions of the samples of the first run (Figure S21b). Variations off the extinctions of all samples stayed within 10%. Additionally, Furlong slopes were calculated from the UV-Vis spectra of the analyzed samples. The calculated Furlong slopes of all samples differed only slightly from each other without any obvious trend as shown in Figure S20c.

7. Electrochemical properties of HEA nanoparticles

As mentioned before, the potential of HEA catalysts for catalyzing the OER in alkaline milieu was tested. Catalysts prepared from colloids produced at different experimental conditions were measured using electrochemical methods, such as cyclic voltammetry (CV) and linear sweep voltammetry (LSV). Additionally, the influence of the mass loading of NPs on the catalyst support and the support material were investigated.

7.1. Reproducibility of the OER activity of HEA/CB catalysts

At first, the systematic deviation of the electrochemical analysis was evaluated. Therefore, three samples from the same ink of a HEA/CB catalyst prepared from a target heat-treated for 20 h (20h_1) were tested. The performance was quantitatively analyzed as NP mass-related current density at the potential of 1.7 V (scan rate: 0.02 V/s) and is presented in Figure S21a. Only small deviations of the current densities were observed, which could be ascribed to slight variations in the electrochemically active surface areas (EASA) of the samples, arising from small changes in the drop casting preparation of the electrodes. The calculated systematic deviation was 5% and was further used to assess the error in the following figures except Figure S22a. Figure S21b shows the OER activities of catalysts prepared from three targets heat-treated for 20 h. Clear differences showed up in their activities for OER. This implied that the choice of the ablation target had a significant influence on the catalytic performance of laser generated HEA NPs, even though the targets were prepared the exact same way. As

shown before, the synthesis of HEA NPs from three different targets heat-treated for a same duration of 20 h (Figure S18) exhibited a high reproducibility.

Figure S21c presents the OER activities of catalysts synthesized from three targets heat-treated for different duration. The error bars represent the maximum deviation of the results shown in Figure S21b. A reduction of the catalytic activity was observed by increasing the target heat-treatment duration from 5 to 50 h. However, the trend lied within the assumable error for using different ablation targets prepared by the method shown in Figure S1.

To investigate the influence of the ablation duration of a single target on the OER activity of HEA catalysts, corresponding catalysts prepared from HEA NPs obtained at different time points during the laser ablation were tested. Figure S21d illustrates that the catalysts prepared from HEA NPs sampled at the 20th and 40th minute of the ablation were as active as the catalyst prepared from NPs sampled in the 3rd minute of ablation. This proves that the consumption of targets due to the ablation within 40 min did not affect the quality of the HEA NPs and the OER activity of catalysts prepared from them. It is also interesting to notice that the consumption of one target induced a lower deviation of the catalytic performance than using different targets.

Conclusively, The OER activity of the samples prepared from a same ink and those synthesized by a long-term ablation exhibited a relatively high reproducibility with weak activity deviations of around 5%. On the contrary, the reproducibility of the OER activity was less satisfactory for samples produced from different targets heat-treated for 20 h (12%) or heat-treated for different durations (12%). This found indicated that one of the early steps in the ablation target production still requires improvement. We assume the mixing procedure of the micropowders to be most prone to introduce inhomogeneity. The chemical composition of the ablation targets should be checked in more and smaller areas of the ablation target surface as it was done in this work. If the reason for the observed activity deviations originated from the target production, inhomogeneity of the elemental distribution must be assumed.

7.2. OER activity tests of differently prepared catalysts

For the following tests, a high amount of HEA NP colloid was produced. All catalyst were prepared from the same batch. HEA/CB catalysts with different loadings of HEA NPs (Figure S22a) were investigated as well as HEA catalysts on different supports (Figure S22b). The mass-related activity decreased steadily by increasing the NP mass loading on CB. When comparing the currents (in mA) normalized to the current of the 20 wt.% catalyst (in mA), as shown in the inlet of Figure S22a, no difference in the performance of catalysts with mass loadings between 10 and 40 wt.% showed up. At even higher loadings, the currents decreased. It can be assumed that the HEA NPs tended to agglomerate on the CB surface and overlapped in multilayers during the adsorption of HEA NPs onto the CB. In this case, the number of the active sites of HEA/CB catalysts could be only slightly changed by increasing the mass loading up to 40 wt.%. By further increasing the loading, a decrease of the active sites of the catalyst or a loss of conductivity due to formation of multilayers probably took place. The exemplary TEM micrographs of different catalysts in Figure S14 show HEA/CB catalysts with different weight

loadings. A stronger agglomeration of the catalysts with higher loadings took place during drying on the TEM grind.

Figure S22b shows the OER activity of HEA catalysts prepared using different support materials. The mass loading was 20 wt.%. Among the tested support materials, CB was the best for the preparation of HEA catalysts leading to the highest activity for OER. The OER activity of HEA/N-GNS was close to that of HEA/CB. HEA/GNS was about one third less active than HEA/CB. HEA/GO exhibited the lowest activity probably due to its oxidized surface. In previous researches, GNS was employed as support material for platinum catalysts to enhance the methanol oxidation reaction, hydrogen oxidation reaction and oxygen reduction reaction.[S3] A higher catalytic activity of Pt/GNS compared to that of Pt/CB was reported. In another study, Pt/GNS was found to be less active in electrochemical catalysis than Pt/CB.[S4] The varying results highlight the differences between the various GNS materials available. Additionally, the dispersion of the HEA catalysts might have varied between the GNS and the CB, leading to different active surface area and thus different activities. The N-doping significantly increased the performances of GNS (as compared to the non-doped), which could be due to enhanced conductivity and the presence of more anchoring defects for NPs. In case of GO, the oxidized surface probably limited the charge transfer between the NPs and the support. The conductivity of GO is lower than that of the other carbon-based materials due to the disruption of its sp2 bonding network.

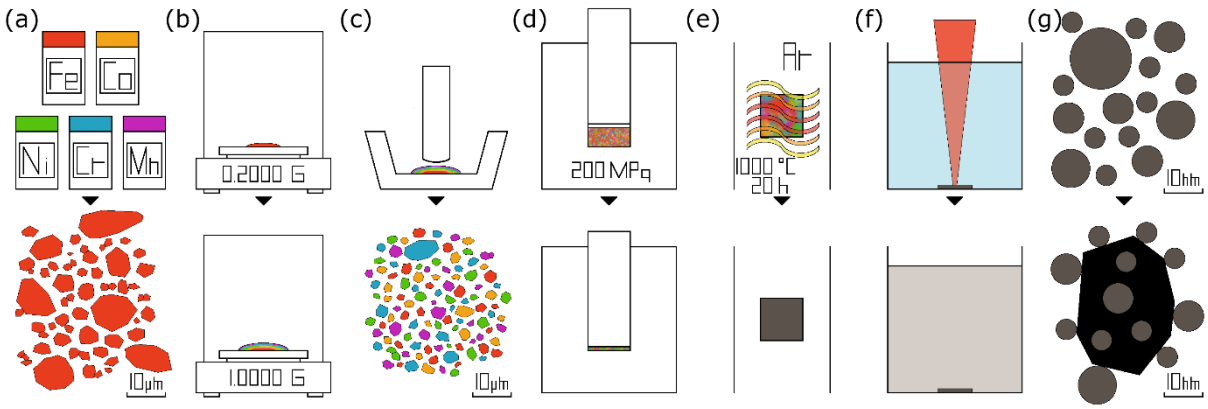

Figure S1. Stepwise documentation of the synthesis of nanoscaled, heterogeneous catalysts from micropowders of single metals. Five single metal micropowders (a), weighing of the single powders (b), grinding and mixing of the powders (c), pressing the powder mixture into a quadratic pellet (d), heat-treatment of the pellet (e), laser ablation of the metal sheet (f) and deposition of as-synthesized nanoparticles on carbon black.

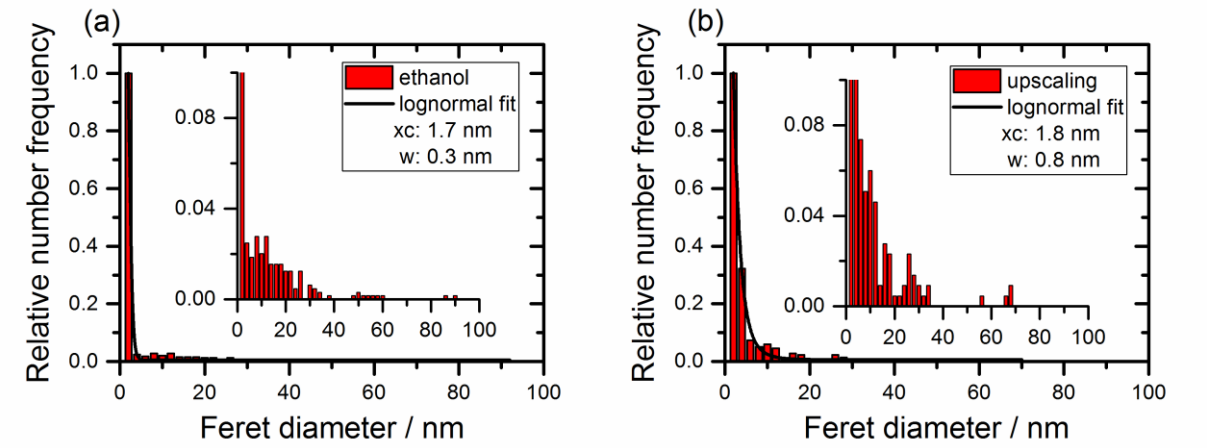

Figure S2. Normalized number frequencies by TEM analysis of nanoparticles yielded by the laser ablation of CoCrFeMnNi in ethanol (a) and in the upscaling approach (b). More than 1,000 particles were measured for both samples.

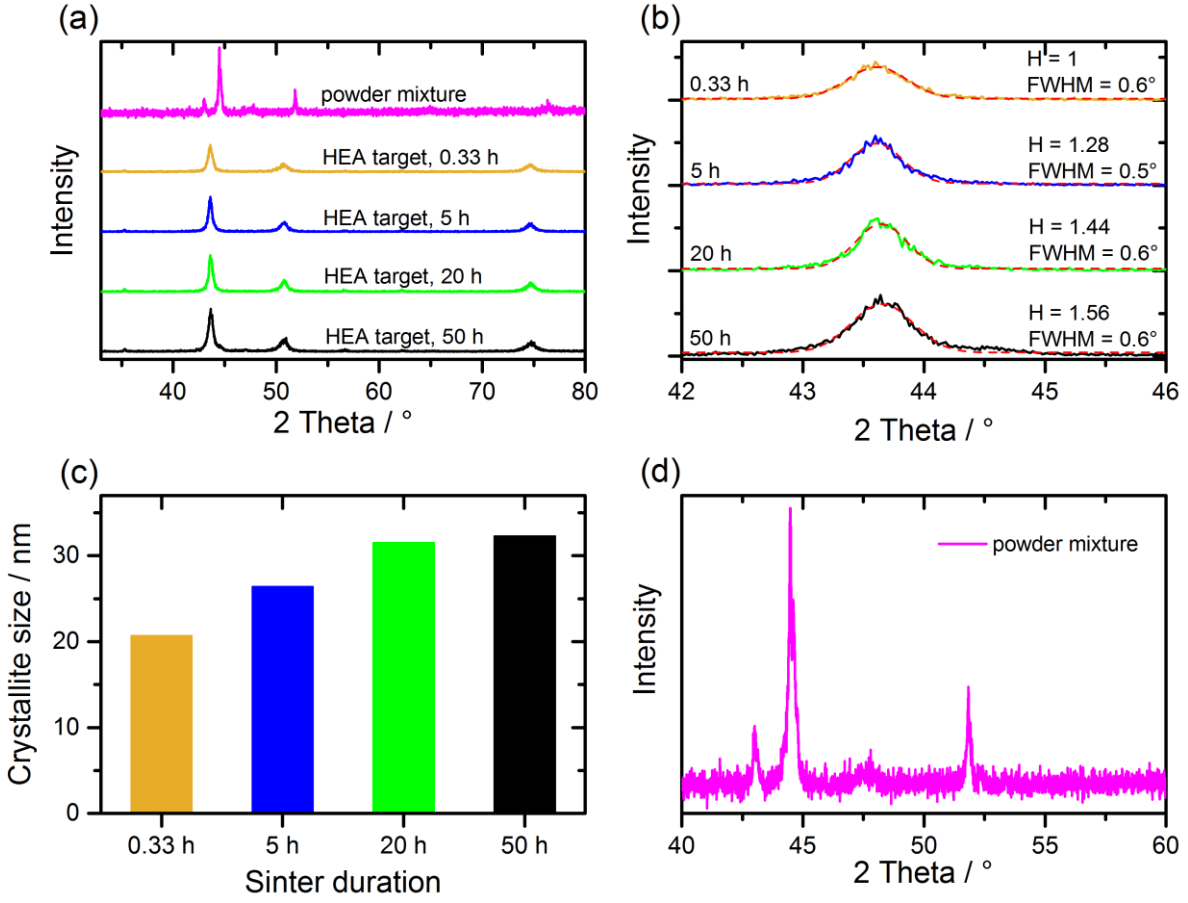

Figure S3. X-ray diffractograms of ablation targets of the CoCrFeMnNi HEA heat-treated for different durations (a), zoomed peaks of the (111) plane of the targets heat-treated for different durations including Gaussian fits (H is the peak height, FWHM the full width at half maximum) (b), the crystallite sizes caused by different target heat-treatment durations (c) and a more detailed presentation of the diffractogram of the powder mixture (d).

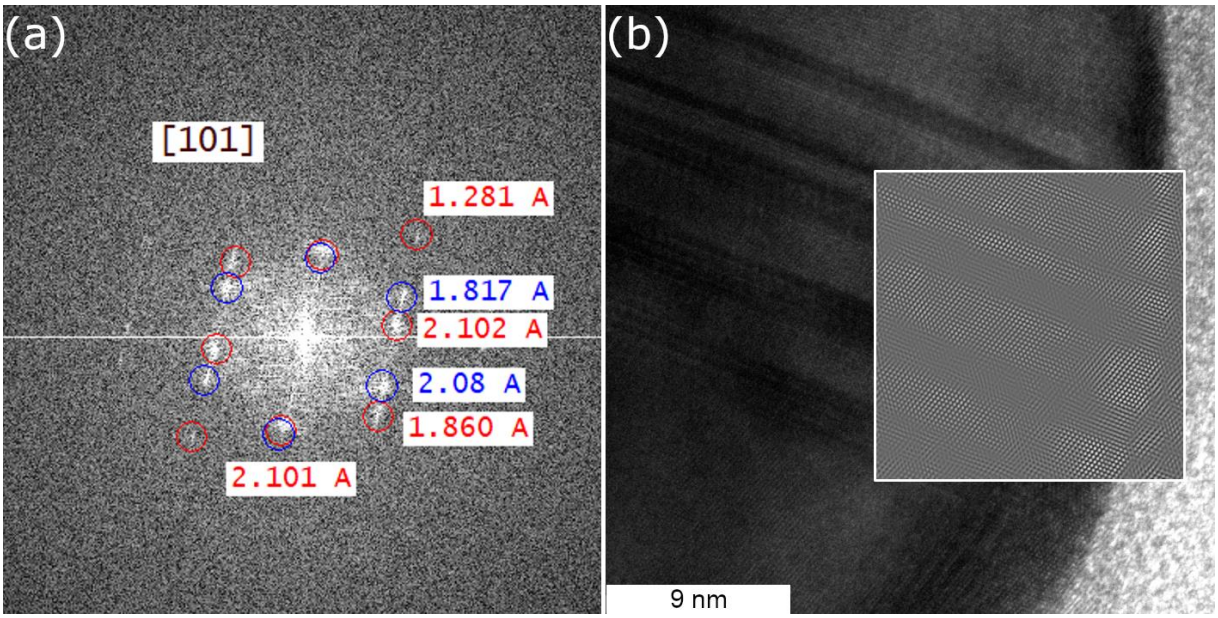

Figure S4. FFT (a) of the lattice ([101] zone axis) (b) of a larger nanoparticle with Σ3-twin formation due to Mn and Cr segregation. The inset in (b) shows the inverse FFT from the blue marked reflections in (a).

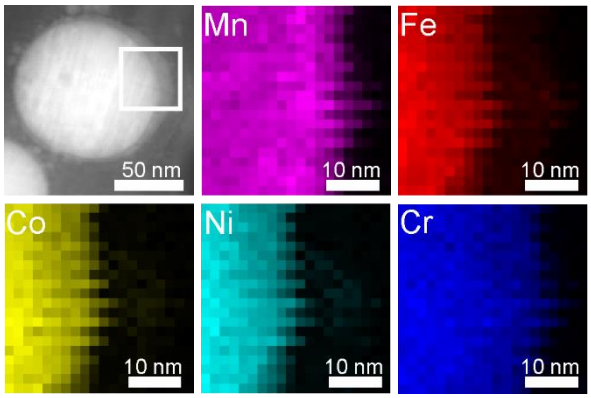

Figure S5. EDX elemental mappings of Mn, Fe, Co, Ni and Cr of the surface region of a larger nanoparticle exhibiting surface segregation of Mn and Cr.

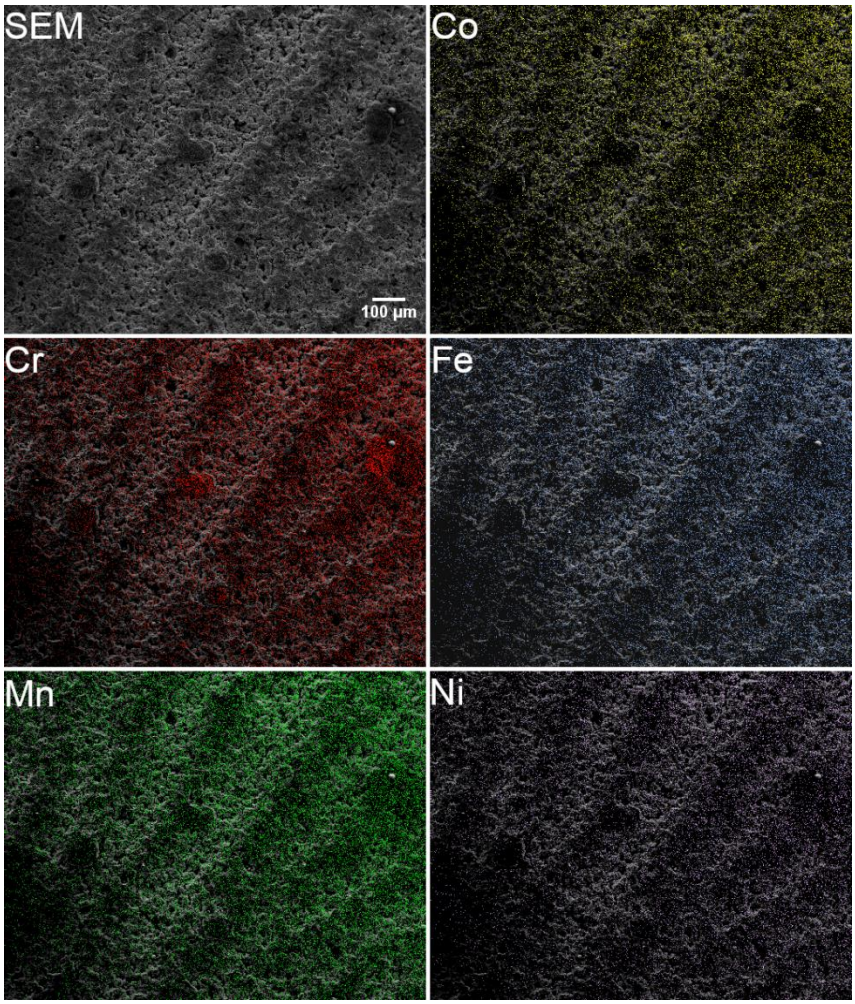

Figure S6. SEM image of the ablation area of a CoCrFeMnNi HEA ablation target and corresponding EDX mapping of Co, Cr, Fe, Mn and Ni. A homogeneous distribution of the single elements was found in the ablation area. Consequently, a homogeneous ablation of all elements took place. The intensity gradient is due to the different distances of the target surface and the EDX detector.

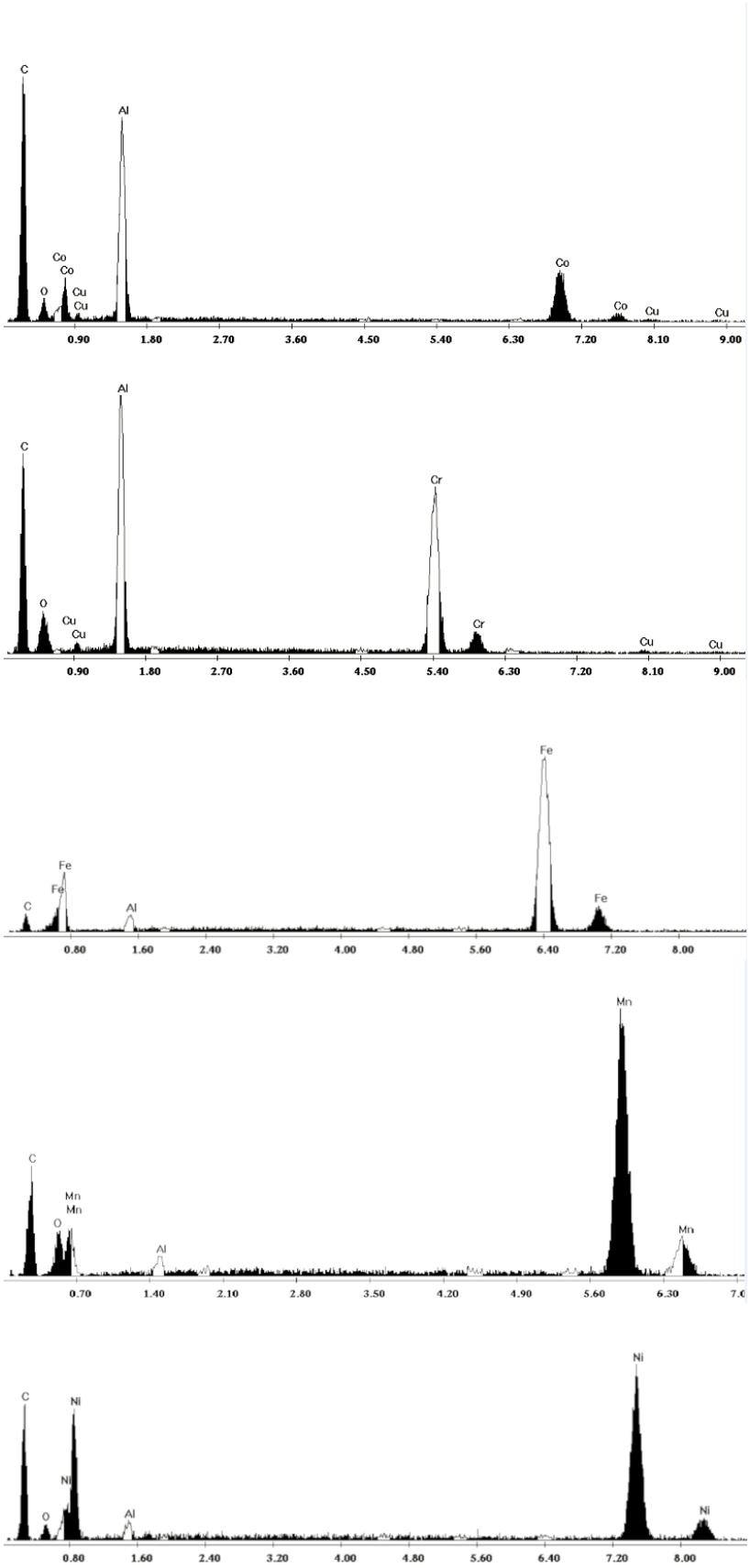

Figure S7. EDX spectra of used Co, Cr, Fe, Mn and Ni micropowders. Energy in keV is on the x-scale and intensity on the y-scale.

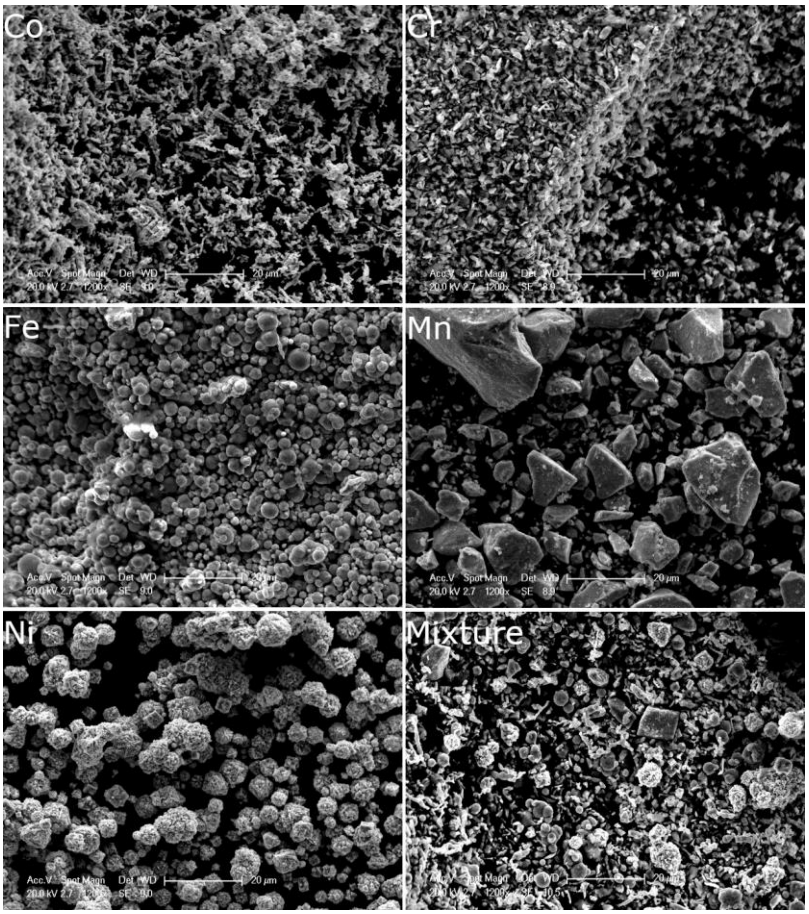

Figure S8. SEM images of used Co, Cr, Fe, Mn and Ni micropowders and their mixture after grinding. Scale bar is 20 µm in each image.

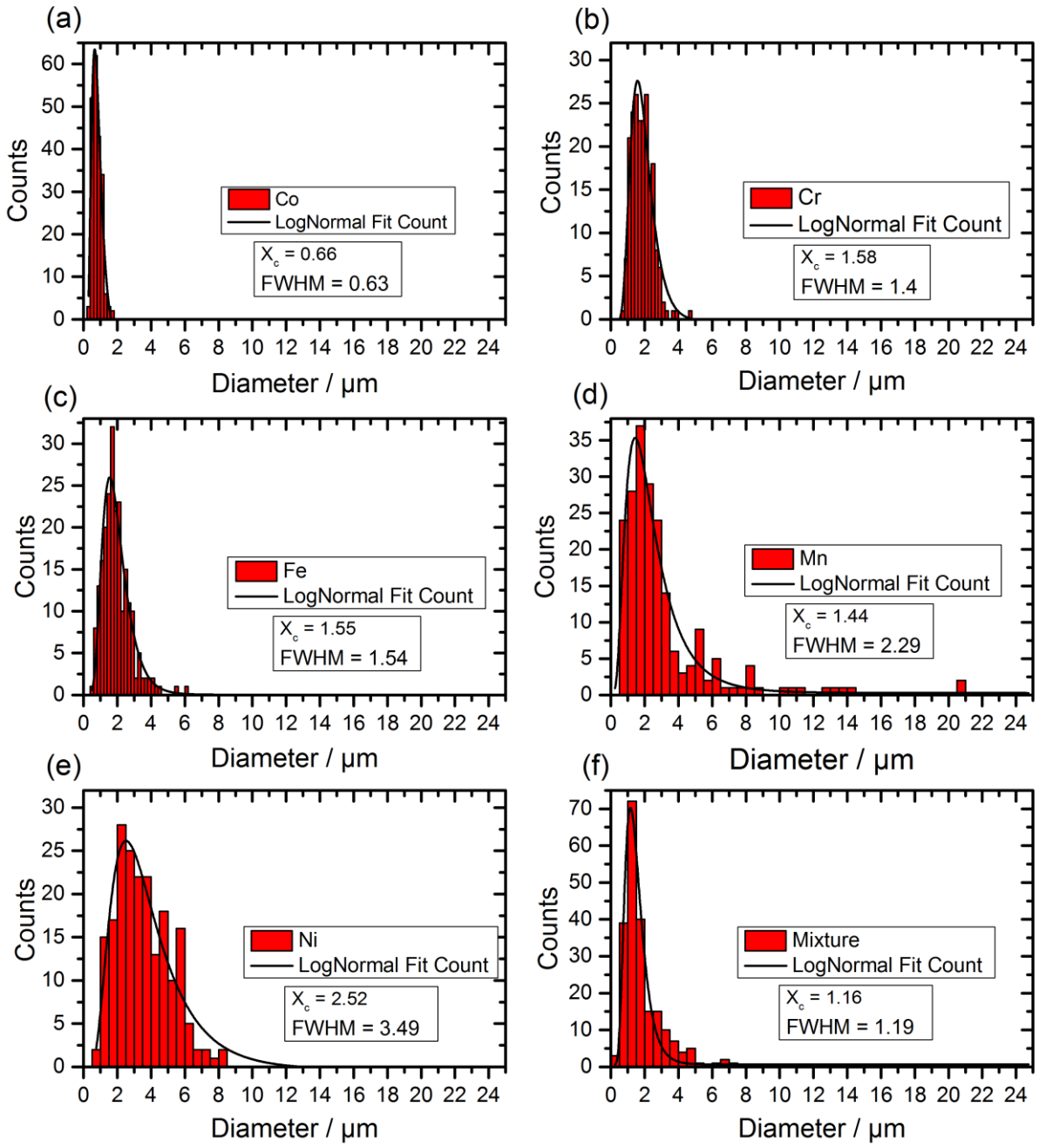

Figure S9. Primary particle size histograms of used Co (a), Cr (b), Fe (c), Mn (d), Ni (e) micropowders and their mixture after grinding (f). X_c is the peak center and FWHM the full width at half maximum. All fit values are given in µm.

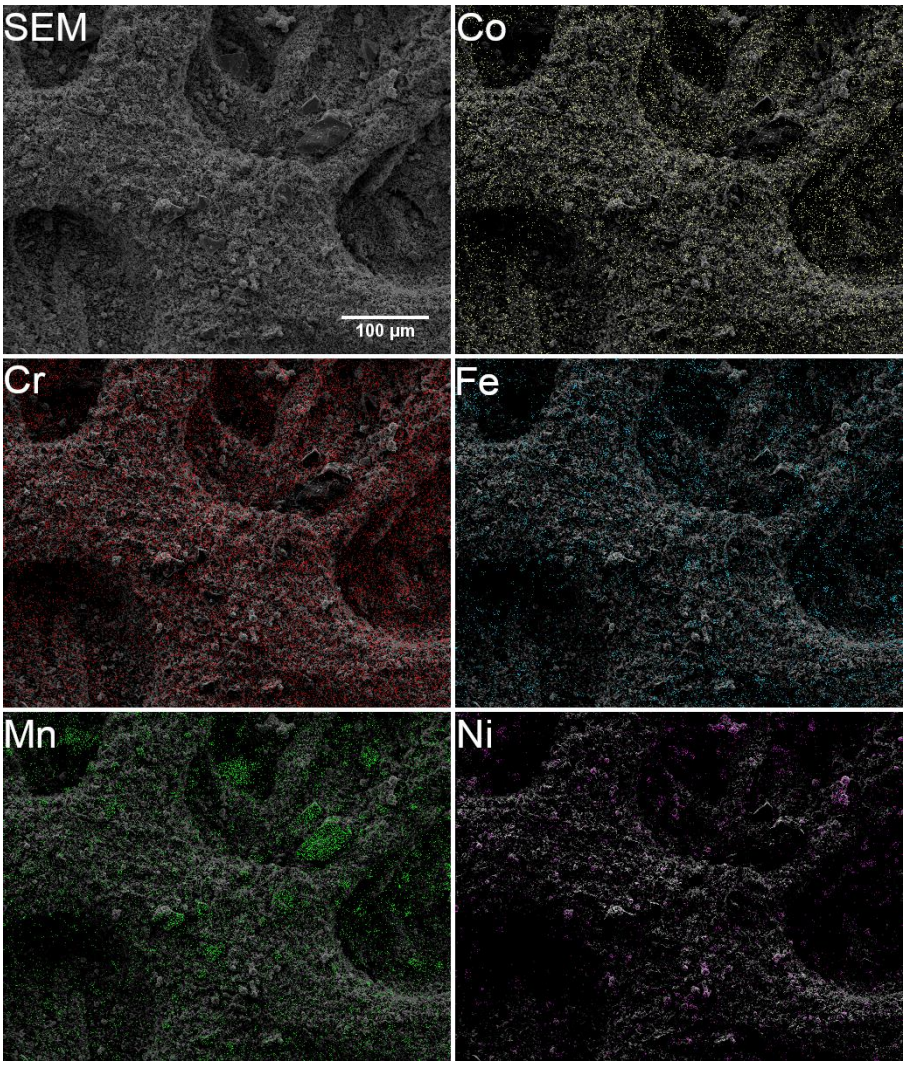

Figure S10. SEM image for a powder mixture after 10 min of grinding, corresponding EDX mapping of Co, Cr, Fe, Mn and Ni. The mixing procedure applied to the micropowders led to a homogeneous mixture of the grains of single elements. However, significantly higher intensities of Mn and Ni were found in single locations due to the presence of some larger grains.

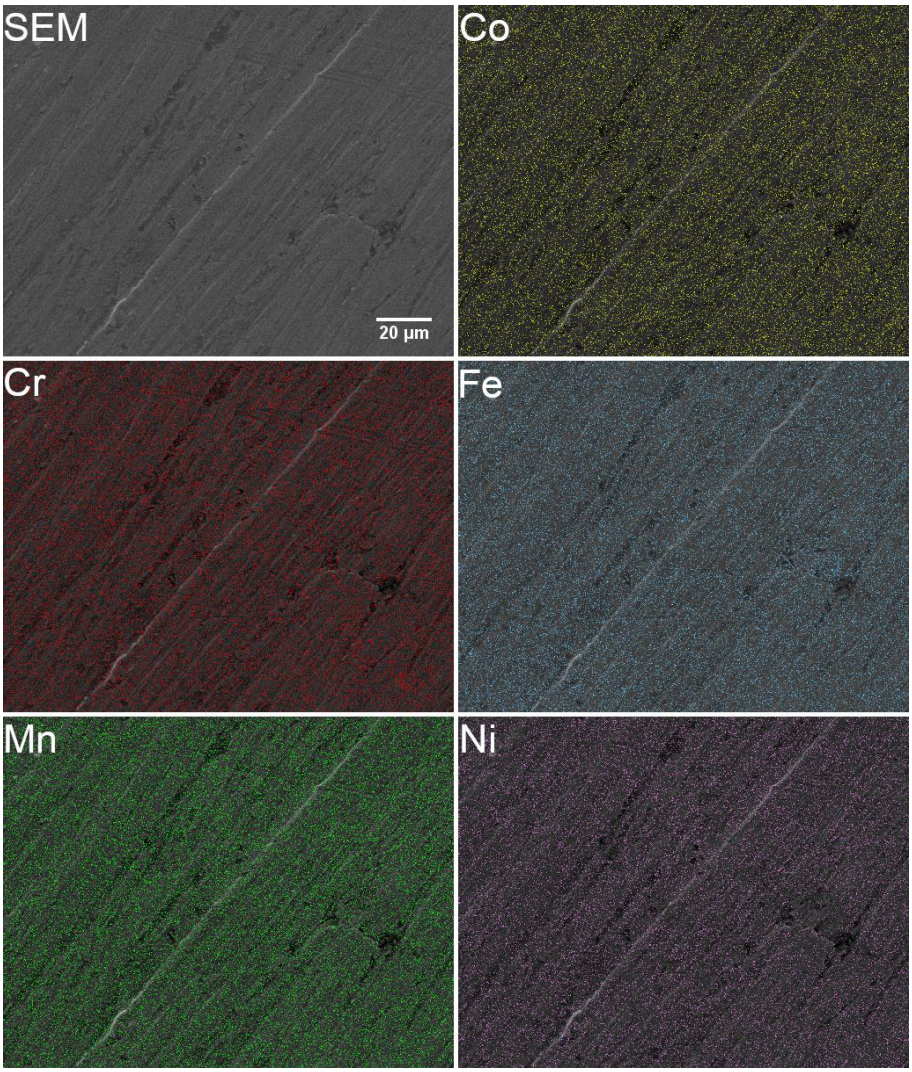

Figure S11. SEM image of a non-ablated target heat-treated for 20 h (a) and corresponding EDX mappings of Co, Cr, Fe, Mn and Ni (b-f). The heat-treatment led to a homogeneous distribution of the single elements in the ablation target.

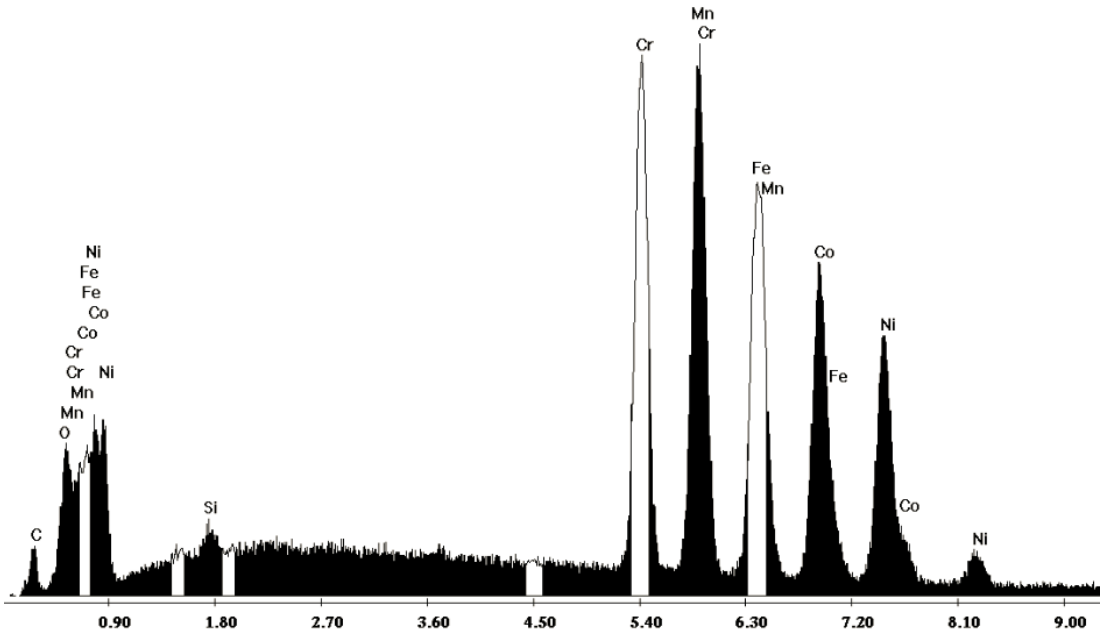

Figure S12. EDX spectrum of an ablation target after 20 h heat-treating and sanding. Energy in keV on the x-scale and intensity on the y-scale.

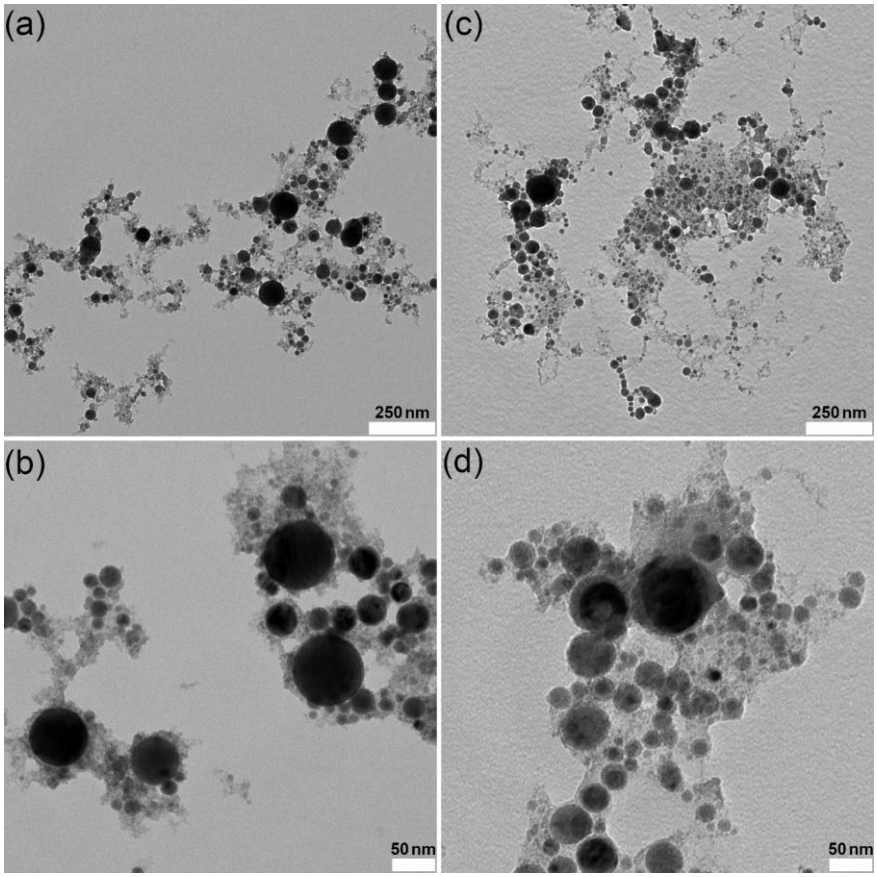

Figure S13. Exemplary TEM images of nanoparticles from the ethanol-based (a, b) and the scaled-up, water-based (c, d) laser ablation of CoCrFeMnNi HEA targets. In ethanol, less oxidation of the nanoparticle surface took place compared to water, as indicated by the less pronounced low-contrast shells around the particles.

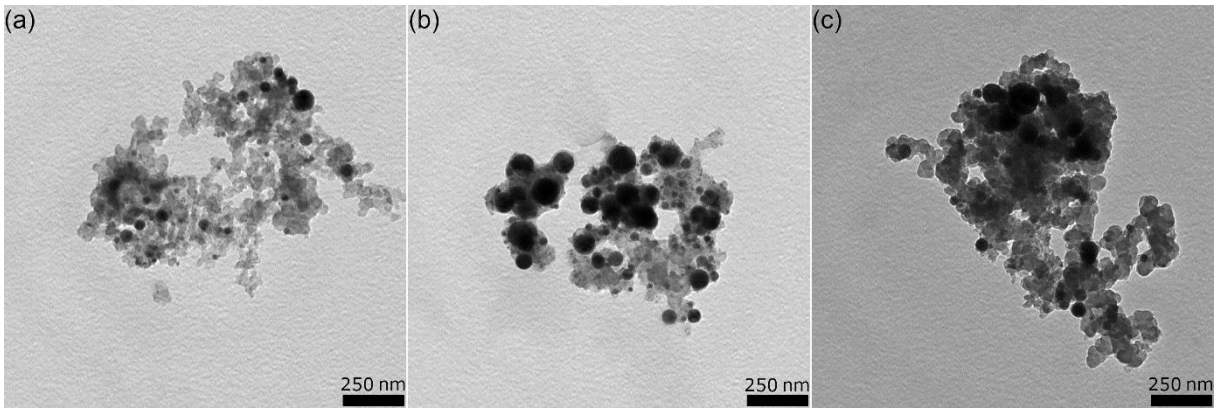

Figure S14. TEM images of 20 wt.% (a), 40 wt.% (b) and 80 wt.% (c) HEA/CB catalysts.

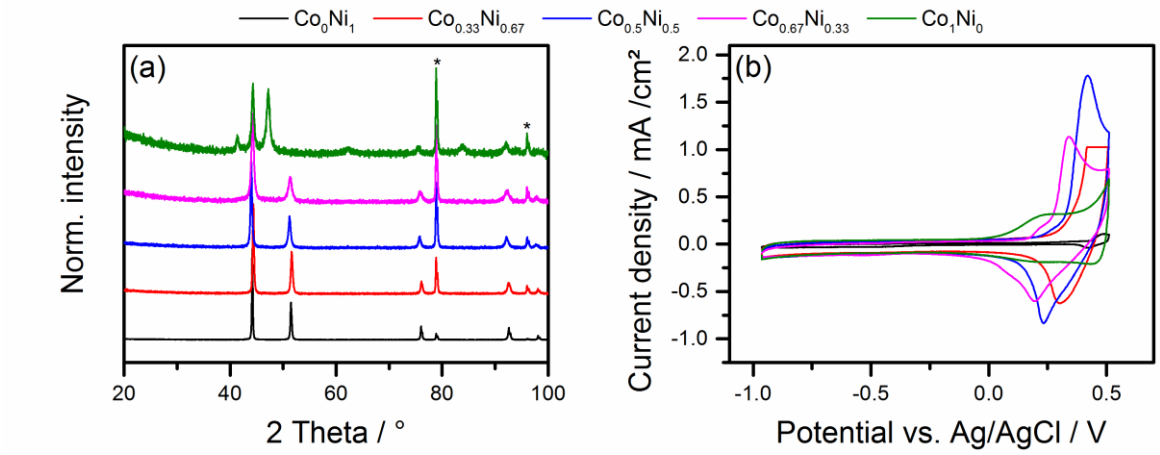

Figure S15. X-ray diffractograms of the ablation targets used for the synthesis of CoNi NPs by laser ablation in water (a) and cyclic voltammograms of catalysts produced from the NPs (b). The asterisks in (a) mark diffraction peaks related to the sample holder.

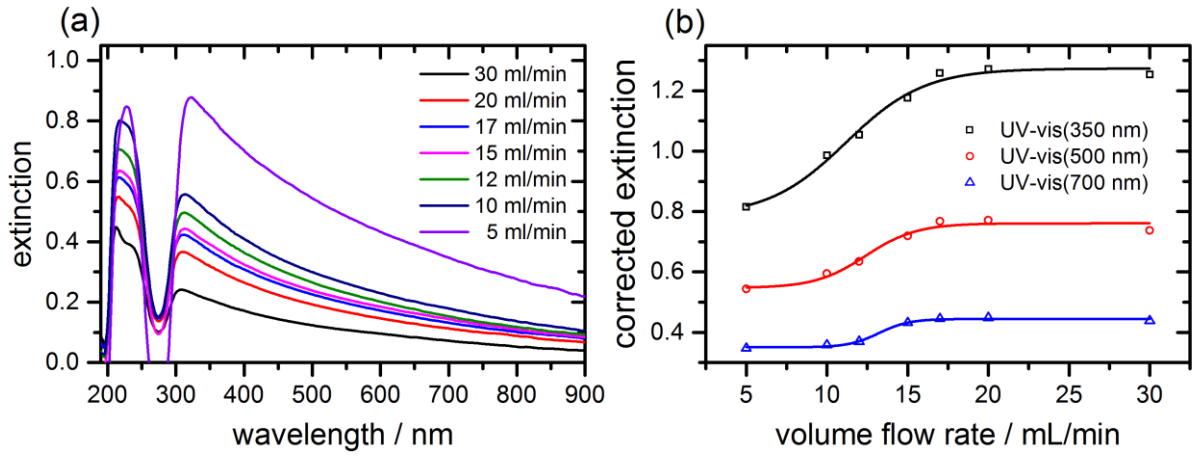

Figure S16. Light extinction spectra of Ni colloids prepared at different volume flow rates (a) and extinctions of these colloids extracted at wavelengths of 350 nm, 500 nm and 700 nm corrected by multiplication with the respective flow rate divided by 5 mL/min versus the volume flow rate (b). The productivity (ablation rate) maximized at volume flow rates in between 15 and 20 mL/min.

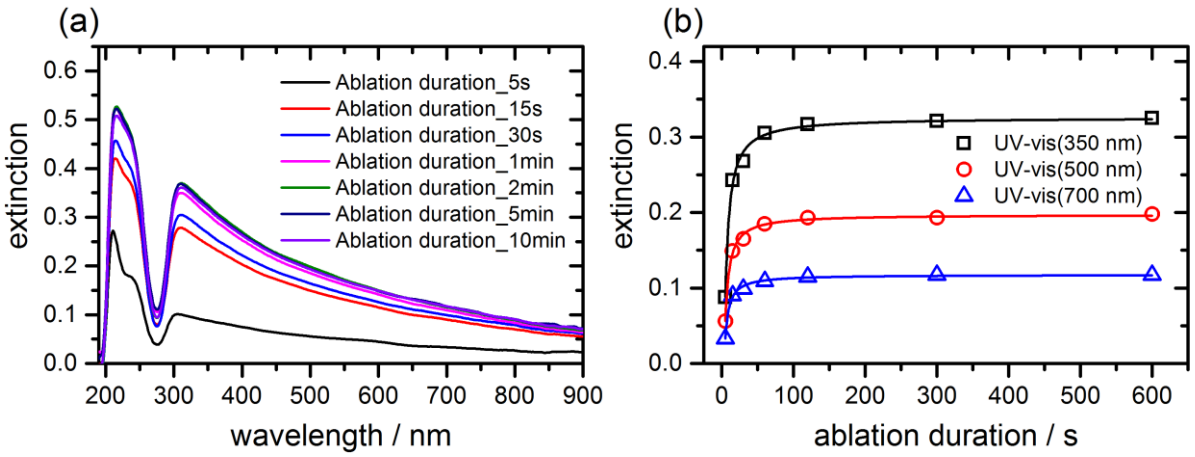

Figure S17. Light extinction spectra of Ni colloids prepared at different ablation durations (a) and extinctions of these colloids extracted at the wavelength of 350 nm, 500 nm and 700 nm versus the ablation duration (b). The concentration of colloidal nanoparticles in the downstream of the ablation chamber saturated after 120 s of the laser ablation process.

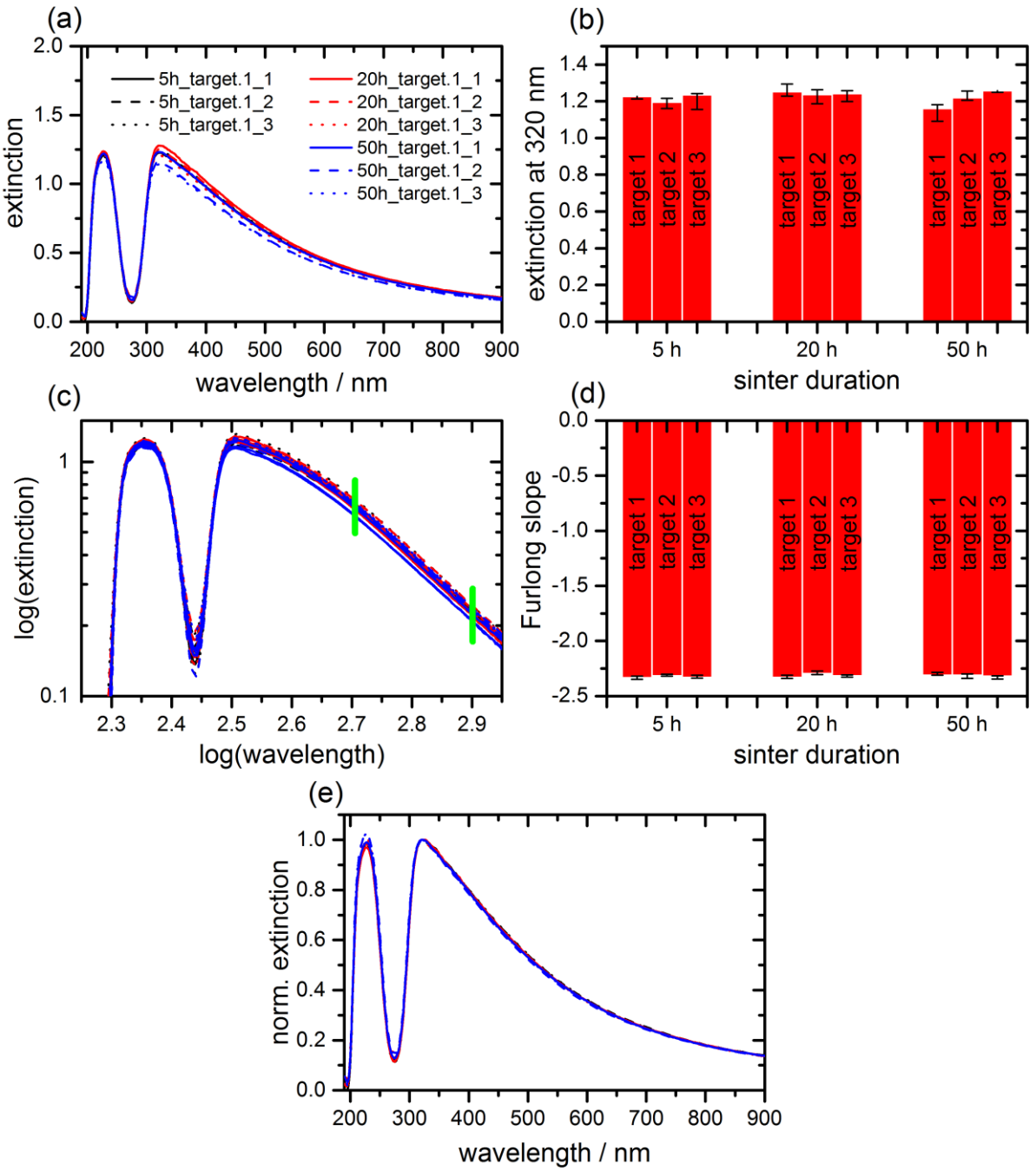

Figure S18. Light extinction spectra of colloids ablated from CoCrFeMnNi high-entropy alloy targets heat-treated for different duration (a), extinctions of these colloids extracted at a wavelength of 320 nm (b), Furlong plots (c), Furlong slopes (d) and normalized light extinction spectra (e) of all colloids. Only data of three colloids produced from one of three targets of each heat-treatment duration are shown in (a), (c) and (e). The legend in (a) is also valid for (c) and (e). Error bars represent maximum deviations derived from three samples. Overall, a high reproducibility of the productivity and the particle size distribution was found by using different HEA targets.

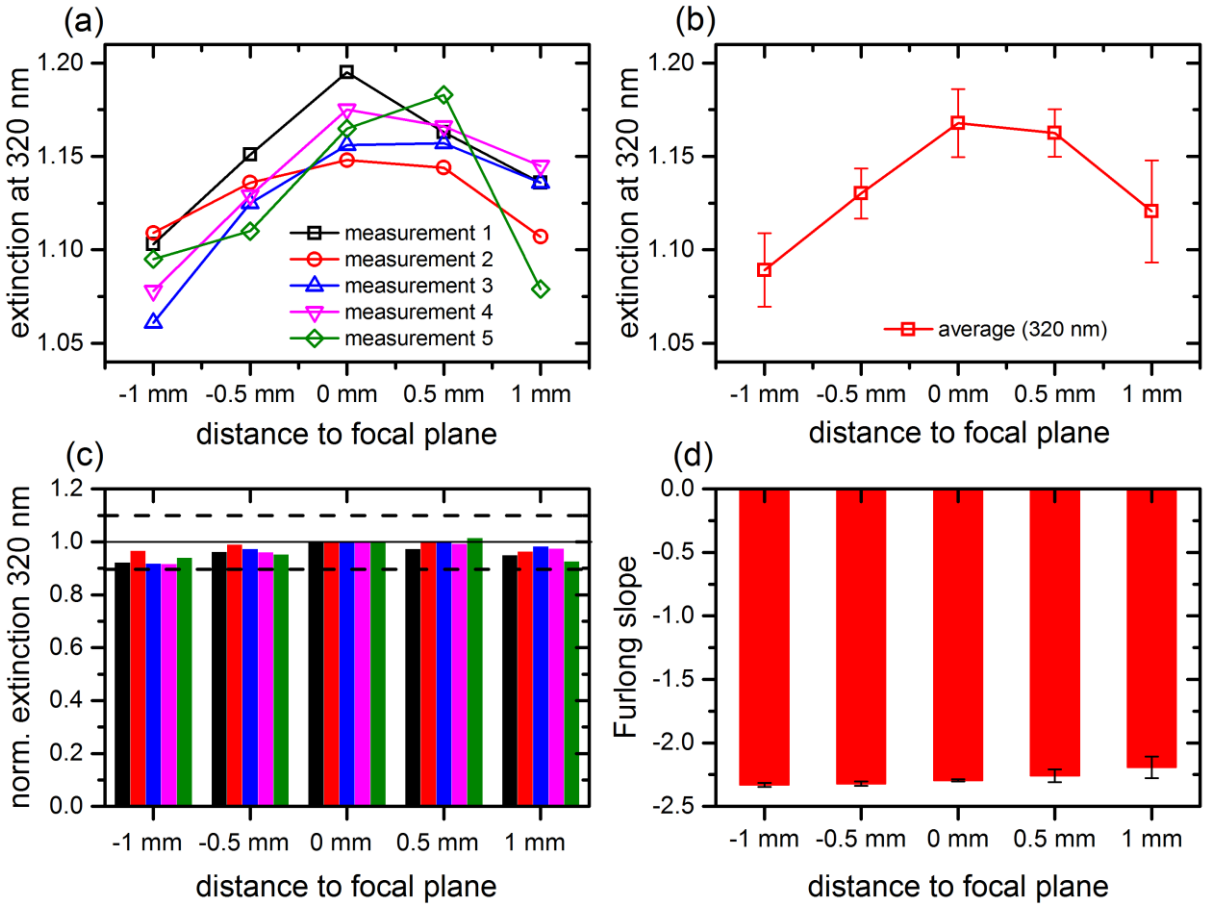

Figure S19. Light extinction data of colloids prepared at different distances to the focal plane positions (a), average (b), normalized extinctions (c) and Furlong slopes (d) of these colloids. A position of 0 mm indicates the highest productivity. At positive values, the focal plane was shifted behind the target surface. The legend in (a) is also valid for (c). Error bars represent the maximum deviations derived from five samples. The working distance between the focusing lens and the ablation target reproducibly affected the productivity and the particle size distribution.

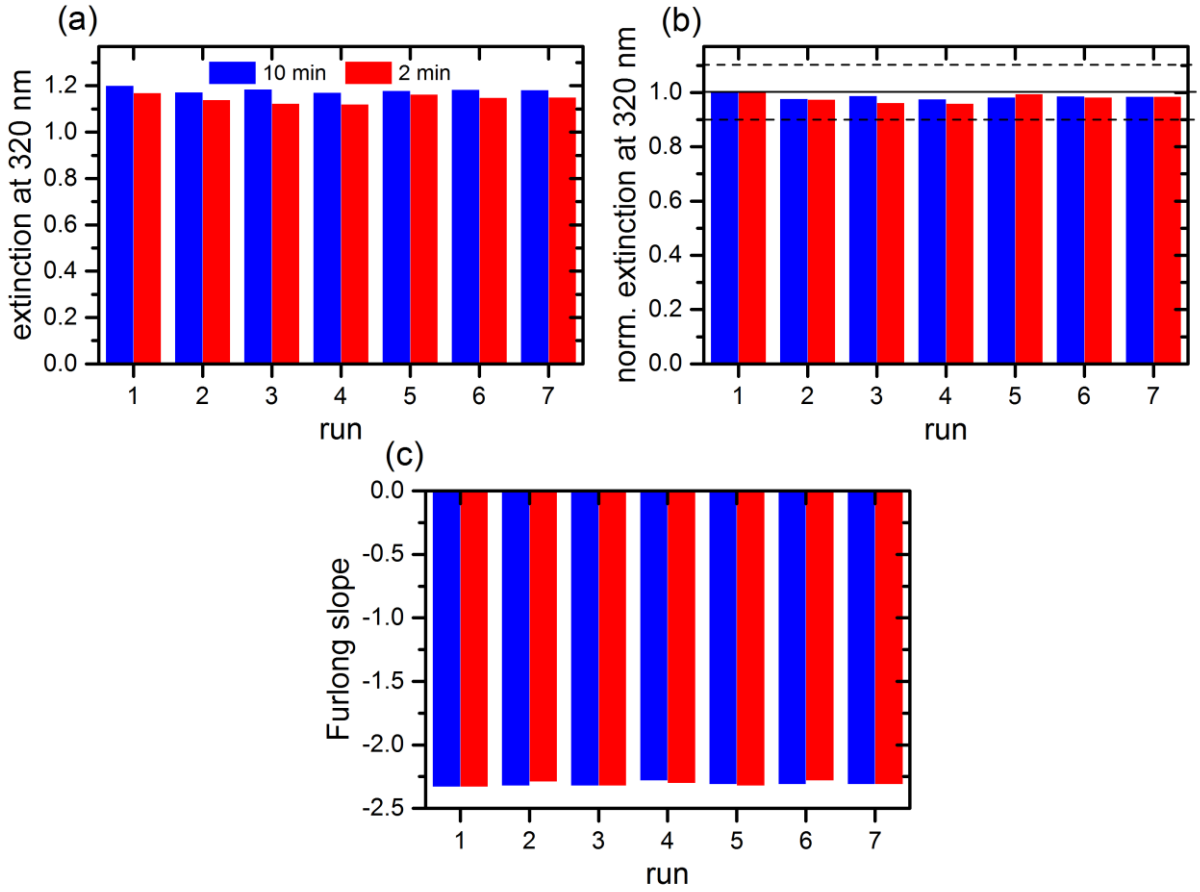

Figure S20. Light extinctions (a), normalized extinctions (b) extracted at a wavelength of 320 nm and Furlong slopes calculated from the light extinction data (c) of colloids sampled 10 min and colloids sampled 2 min after a restart of the laser ablation process. The legend in (a) is also valid for (b) and (c). A high reproducibility of the productivity and the particle size distribution was found during several restarts of the ablation process.

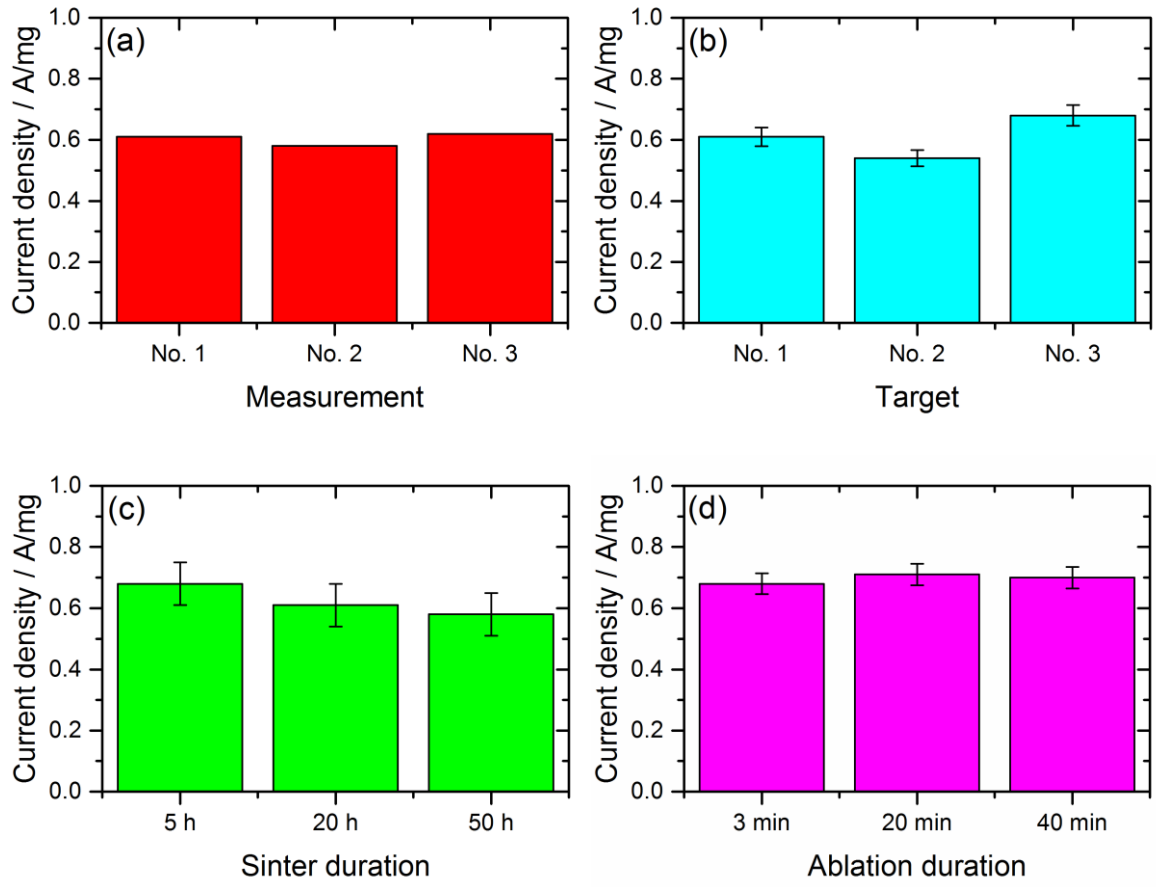

Figure S21. OER activities of three coatings of the electrode prepared from the same ink of a HEA/CB (a), of three catalysts prepared from three different targets heat-treated for 20 h (b), of three catalysts prepared from three targets heat-treated for different durations (c) and of three catalysts prepared after different durations of laser ablation. The ablation time did not affect the catalytic activity of the nanoparticles. A significant influence of the ablation target on the catalytic activity was found.

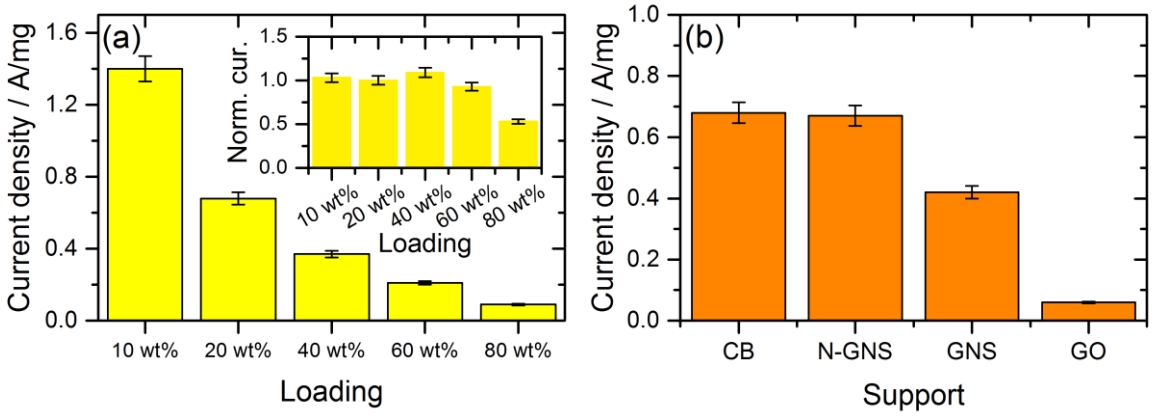

Figure S22. OER activities of HEA/CB catalysts with different weight loadings of HEA NPs (a) and OER activities of HEA catalysts with different supports (b). Inlet in (a) shows the normalized current. The current was normalized to the current measured for the 20 wt.% catalyst. The nominal current provided by a catalyst was independent from the mass loading of nanoparticles on the carbon support in the range of 10 to 40 wt.%. NPs on carbon black (CB) and nitrogen-doped graphene nanosheets (N-GNS) performed better in OER catalysis than NPs on GNS and graphene oxide (GO).

References

S1 F. T. L. Muniz, M. A. R. Miranda, C. M. dos Santos and J. M. Sasaki, *Acta Crystallogr. A,* 2016, **72**, 385.

S2 D. N. Furlong, A. Launikonis, W. H. F. Sasse and J. V. Sanders, *J. Chem. Soc., Faraday Trans. 1,* 1984, **80**, 571.

S3 R. Siburian and J. Nakamura, *J. Phys. Chem. C,* 2012, **116**, 22947.

S4 Y. S. Yun, D. Kim, Y. Tak and H.-J. Jin, *Synth. Met.,* 2011, **161**, 2460.